

## High-statistics study of $\pi^+p$ , $\pi^-p$ , and $pp$ elastic scattering at 200 GeV/c

A. Schiz,\* L. A. Fajardo, R. Majka,† J. N. Marx,† P. Némethy,† L. Rosselet,‡ J. Sandweiss, and A. J. Slaughter  
Yale University, New Haven, Connecticut 06520

C. Ankenbrandt, M. Atac, R. Brown,§ S. Ecklund,|| P. J. Gollon,¶ J. Lach, J. MacLachlan, A. Roberts, and G. Shen\*\*  
Fermi National Accelerator Laboratory, Batavia, Illinois 60510

(Received 10 December 1979)

We have measured  $\pi^+p$ ,  $\pi^-p$ , and  $pp$  elastic scattering at an incident-beam momentum of 200 GeV/c in the region of  $-t$ , four-momentum transfer squared, from 0.021 to 0.665 (GeV/c)<sup>2</sup>. The data allow an investigation of the  $t$  dependence of the logarithmic forward slope parameter  $b \equiv (d/dt)(\ln d\sigma/dt)$ . In addition to standard parametrizations, we use functional forms suggested by the additive quark model to fit the measured  $d\sigma/dt$  distributions. Within the context of this model we estimate the size of the clothed quark in the pion and proton. Limits on the elastic-scattering amplitude derived from unitarity bounds are checked, and no violations are observed.

### I. INTRODUCTION

The distribution in  $t$ , four-momentum transfer squared, for elastic scattering of hadrons provides information about the character of the strong interaction. In an optical model this distribution is dependent on the sizes and opacities of the interacting particles. The additive quark model (AQM) derives  $d\sigma/dt$  from a simple quark-quark interaction modified by form factors which reflect the spatial distribution of the quarks inside the interacting hadrons. In a Regge model this distribution depends on the structure of the Pomeron and of any other exchanges which contribute to elastic scattering.

Data from early experiments<sup>1</sup> at  $-t < 0.8$  (GeV/c)<sup>2</sup> and at moderate energies (5 to 30 GeV) were fit with a simple exponential function of  $t$ :

$$\frac{d\sigma}{dt} = A e^{bt}, \quad (1)$$

where  $b$  is independent of  $t$ . However, later results from experiments at Fermilab,<sup>2,3</sup> SLAC,<sup>4</sup> and the CERN ISR (Ref. 5) show a more complicated  $t$  dependence of  $d\sigma/dt$ . An exponential with a quadratic term

$$\frac{d\sigma}{dt} = A e^{bt+ct^2} \quad (2)$$

gives a good representation of the Fermilab data taken with beam energies between 50 and 175 GeV in the intermediate  $t$  range [ $0.05 < -t < 1.0$  (GeV/c)<sup>2</sup>]. Very precise data at 10 and 14 GeV from SLAC show an even more complicated  $t$  dependence, while the ISR results suggest a break in the  $t$  distribution for proton-proton scattering. Finally, data from the CERN SPS (Ref. 6) on the logarithmic forward slope in the small- $t$  region

$[-t < 0.05$  (GeV/c)<sup>2</sup>] are inconsistent with extrapolated values of the slope as derived from data in the intermediate  $t$  range.

We have made a high-statistics study of  $\pi^-p$ ,  $\pi^+p$ , and  $pp$  elastic scattering at 200 GeV/c incident momentum. The  $t$  range is from  $-0.021$  to  $-0.665$  (GeV/c)<sup>2</sup> (scattering angles from approximately 0.7 to 4 mrad). Thus in a single experiment we measure  $d\sigma/dt$  over the small-to-intermediate- $t$  region.

The high statistics allow us to make a detailed study of the shape of the elastic-scattering  $t$  distributions. We will present the  $t$  dependence of  $b$ , the logarithmic slope parameter, defined as

$$b(t) \equiv \frac{d}{dt} \left( \ln \frac{d\sigma}{dt} \right). \quad (3)$$

In addition to standard parametrizations, we use functional forms suggested by the AQM to fit the measured  $d\sigma/dt$  distributions. We also check limits on the elastic-scattering amplitude derived from unitarity bounds.

### APPARATUS

The experiment was performed in the M6 West beam line<sup>7</sup> of the Meson Lab at Fermilab. The apparatus, shown in Fig. 1, is a high-resolution spectrometer which detects the forward particle. The apparatus is described in detail in Ref. 8; therefore, this section will review only the salient features.

The beam line consisted of three stages, each having point-to-parallel-to-point focusing (only the latter two stages are shown in Fig. 1). The beam was momentum-dispersed at the second focus. There a proportional wire chamber (PWC) with 1-mm wire spacing measured the incident momen-

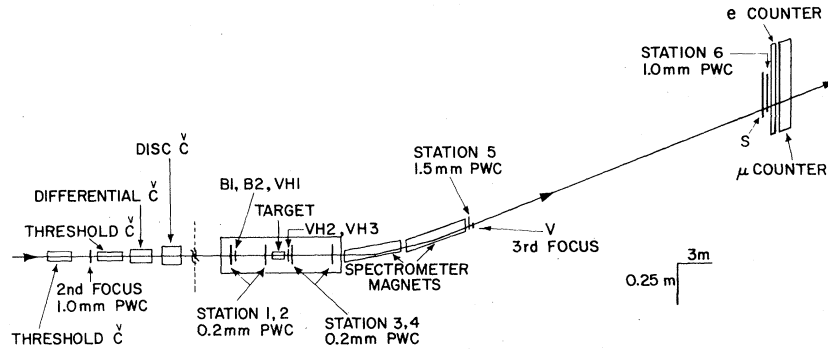


FIG. 1. Plan view of experimental apparatus. (Not to scale left of vertical dashed line.)

tum  $p_i$  with a precision of 0.05% for  $\Delta p_i/p$  relative to the central beam momentum  $p$ . The errors and uncertainties quoted in this paper are standard deviations.

Four Čerenkov counters identified pions, kaons, and protons. From the Čerenkov pressure curves, we determined that the contamination of the kaon signal by pions and protons was less than 0.5%. The small contamination of electrons and muons in the beam was tagged at the downstream end of the experiment.

The liquid-hydrogen ( $\text{LH}_2$ ) target, 52.7 cm in length, and the PWC's to measure the scattering angle, were located downstream of the Čerenkov counters in the third stage of the beam. The above were mounted on a large reinforced concrete block for stability. Beam-defining scintillation counters  $B1$  and  $B2$  and the veto  $VH1$ , were located at the upstream end of the concrete block. Immediately downstream of the target two scintillation counters  $VH2$  and  $VH3$  were used to suppress unwanted scatters from target electrons and hadronic inelastic scatters. Two stations of high-resolution, high-pressure PWC's on either side of the  $\text{LH}_2$  target (stations 1–4 in Fig. 1) measured the scattering angle. At each station a measurement was made of the track's horizontal ( $x$ ) and vertical ( $y$ ) coordinates. In addition, station 3 measured the track along the  $u$  and  $v$  directions (rotated 45 and 135 degrees from the horizontal). The chambers had a 70- $\mu\text{m}$  resolution, and the resulting scattering angles were measured to 30  $\mu\text{rad}$ .

The spectrometer magnets used to determine the momentum of the scattered particle were two dipoles of the type used in the Fermilab main ring. The magnet aperture was nearly rectangular with horizontal and vertical dimensions of 10 and 5 cm. Measurements of the integrated field were made over the magnet aperture; these showed the field to be uniform to 0.04%. A particle with momentum

equal to the beam central momentum was bent 34 mrad in the horizontal plane.

A scintillation counter  $V$  was placed at the third focus, or veto plane, of the beam. Figure 2 shows the placement of this counter relative to the beam center and relative to the projection of the aperture of the last spectrometer magnet onto the veto plane. Unscattered beam tracks and scatters with  $-t < 0.01$  ( $\text{GeV}/c$ )<sup>2</sup> were vetoed by this counter. The counter shape was chosen to provide a relatively uniform acceptance in  $t$ .

At the end of the apparatus were a pair of PWC's with an effective wire spacing of 1 mm. Using these PWC's in conjunction with stations 3 and 4, the outgoing momentum  $p_f$  was measured to a precision of 0.1% ( $\Delta p_f/p$ ) relative to the central momentum.

#### DATA ACQUISITION

The data-collection logic consisted of a two-level trigger. The first level used the various

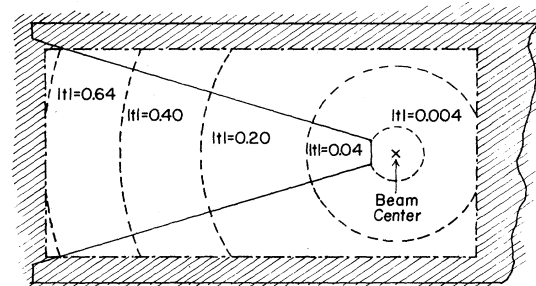


FIG. 2. Veto-plane geometry, elevation view with beam direction into the figure. The solid line denotes counter  $V$ , the shaded region denotes the projection of the downstream spectrometer magnet onto the veto plane. The dashed circles indicate the  $|t|$  of a scattered particle originating on the beam center. The average beam spot size was approximately 3.0 mm full width at half maximum vertically but 4.5 mm FWHM horizontally. The aperture is 5 cm (vertical)  $\times$  10 cm (horizontal).

scintillation counters. The second level used the high-resolution PWC's and an analog calculator called the hardware focus scatter detector (HFSD).<sup>9</sup> An event that satisfied both levels is called a "scatter."

The first level of the trigger for a scatter consisted of the following requirements on the scintillator counters:

- (1) a reasonable incoming beam trajectory defined by  $B1 \cdot B2 \cdot \sqrt{HI}$  and other beam-defining counters in the second beam stage (not shown in Fig. 1),
- (2) a unique particle identification by the Čerenkov counters,
- (3) no other incident particle within  $\pm 400$  nsec of the trigger,
- (4) a signal from  $S$  (at the end of the apparatus), and
- (5) no signal from the veto  $V$  at the beam third focus.

The second level of trigger was needed since the first level was dominated by the beam halo. The HFSD performed simultaneously two calculations, called HFD and HSD, using the track coordinates as measured in the high-resolution PWC's. Figure 3 schematically presents the two calculations. In the HFD test the incoming track, as extrapolated from the coordinates measured in the two high-resolution PWC's upstream of the target (stations  $A$  and  $B$  in Fig. 3), was required to intercept a preset window in the veto plane. This HFD requirement was imposed in both the  $x$  and  $y$  projections to eliminate beam halo. The HFD test also rejected events with spurious coordinates in the first two stations that would fool the HSD test. The HSD test required that the data from the two upstream and the most downstream high-resolution chambers ( $A$ ,  $B$ , and  $C$  in Fig. 3) represent the projected angle of a scatter with  $-t$  greater

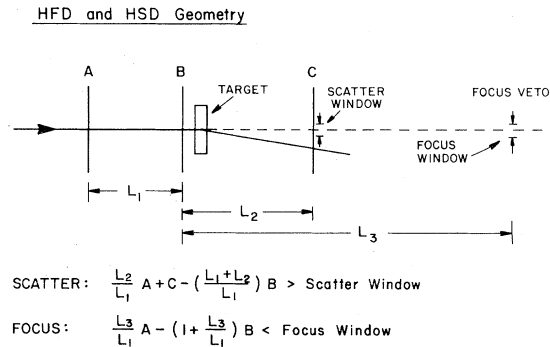


FIG. 3. Schematic presentation of HFSD operation.  $L_1 = 3.5$  m,  $L_2 = 7.0$  m, and  $L_3 = 20.8$  m. The minimum scattering angle accepted by the HSD was set to approximately  $245 \mu\text{rad}$  or  $-t < 0.01$   $(\text{GeV}/c)^2$ . In Fajardo *et al.* (Ref. 8), it was approximately  $0.001$   $(\text{GeV}/c)^2$ .

than  $0.01$   $(\text{GeV}/c)^2$ . Although the HSD test was made in the vertical and horizontal projections, the second-level trigger required that only one projection passed the HSD test. The analog processor took about  $5 \mu\text{sec}$  to make its decision, and reduced the trigger rate by approximately 66%.

Two additional trigger types were recorded along with the scattered events; in neither was the HFSD required. The first additional trigger, called "beam," was a sample of beam particles that passed the first three requirements of the first level. These triggers provided information for alignment and normalization and the incident-beam phase space for the Monte Carlo simulation.

The second was a specified fraction of events satisfying the first level of the trigger. These events, called prescaled accepted events (PAE's) were used to study the HFSD performance and any biases it may have introduced into the data; no such biases were found.

The data were accumulated over a two-week period. The accelerator operated at 400 GeV with a repetition rate of 10 sec and a 1-sec spill time. The beam contained typically  $5 \times 10^5$  particles per accelerator pulse. Approximately 400 triggers were recorded per second; out of these approximately 40 were beam events, approximately 10 PAE's, and the remainder scatters. The relative fraction of events recorded involving a particular particle type was scaled to result in an apparatus live time of 60%.

#### DATA REDUCTION

We used the quantity  $q$  in the analysis where

$$q = \sqrt{-t} \approx P_b \theta, \quad (4a)$$

where  $P_b$  = beam momentum,  $\theta$  = scattering angle, and

$$\frac{d\sigma}{dq} = -2\sqrt{-t} \frac{d\sigma}{dt}. \quad (4b)$$

There are two reasons for this choice. The first is that the resolution of the apparatus was constant in  $q$ , with a standard deviation of 6.0 MeV/c, making it natural to bin events according to  $q$ . The second reason is that  $d\sigma/dq$  over equal  $q$  bins is a more slowly varying function than  $d\sigma/dt$  over equal  $t$  bins. Thus  $d\sigma/dq$  populates the bins more uniformly, thereby reducing the sensitivity of the fitting procedure to the following effects: (1) integration of the cross section over the bin, and (2) the migration of events from bin to bin due to resolution.

The data-reduction process kept only events with unambiguous single tracks before and after the  $\text{LH}_2$  target. This requirement had to be ful-

TABLE I. Major cuts to extract elastic signal.

Cut	Fractions of events remaining after cut		
	$\pi^-$	$\pi^+$	$p$
(1) Track-reconstruction requirements on PWC coordinates and HFD test passed.	0.446	0.545	0.546
(2) No count from <i>VH2</i> and <i>VH3</i> .	0.368	0.457	0.447
(3) HSD test passed.	0.366	0.455	0.447
(4) Scattering angle in $x$ and $y$ projections $\geq .25$ mrad.	0.355	0.444	0.443
(5) Track $\leq 1.5$ cm from center of PWC station 4.	0.352	0.438	0.440
(6) Outgoing particle trajectory traversed the area inside of spectrometer magnet apertures.	0.342	0.427	0.430
(7) Scatter vertex no more than 40 cm beyond $LH_2$ target ends.	0.293	0.361	0.375
(8) $0.0 \leq$ recoil mass squared $\leq 1.76$ (GeV/ $c^2$ ) <sup>2</sup> .	0.215	0.272	0.287
(9) Events whose trajectories were in region of $>90\%$ efficiency in PWC station 4.	0.167	0.254	0.269
(10) Outgoing particle trajectory did not traverse the area of the counter <i>V</i> at the third focus.	0.120	0.217	0.231

filled by both scatter and beam events. Data-summary tapes were produced which contained the relevant kinematic quantities ( $q$ , scattering vertex position, etc.) of each event; cuts were then applied to extract the elastic scattering signal. The alignment procedure used a subset of beam events that had one and only one hit (a set of activated contiguous wires) per PWC.

The target-full and target-empty  $q$  distributions,  $N_s^F(q)$  and  $N_s^{MT}(q)$ , respectively, were normalized and then a target-empty subtraction was performed:

$$N_s(q) = \frac{N_s^F(q)}{I_0^F} - \frac{N_s^{MT}(q)}{I_0^{MT}}.$$

Here  $I_0^F$  and  $I_0^{MT}$  are the total incident-beam fluxes for the target-full and -empty runs. The target-full and target-empty beam events were well-known fractions of all incident particles for both the target-full and target-empty data samples, respectively. Unscattered beam particles and the fast-forward particles from elastic scatters were affected in the same way by absorption in the target and downstream of the target and by overall PWC inefficiencies in the chambers downstream of the target. Thus by using beam events that traversed the entire apparatus to calculate  $I_0^F$  and  $I_0^{MT}$ , these corrections affect both the numerator and the denominator in the same manner and hence cancel. The target-empty subtraction was a 1–2% effect in the lowest- $q$  bins and negligible elsewhere.

The major cuts applied to extract the elastic signal are given in Table I. We found that approximately 20% of the  $\pi^+p$  and  $pp$  triggers and 15% of the  $\pi^-p$  triggers survived the cuts. Half the trig-

gers were eliminated by track reconstruction cuts imposed on the hits in the PWC's. The rest of the rejected triggers failed one or more cuts on the kinematic quantities associated with the scatter. The most important of these were the requirements that the scatter vertex occur in the region of  $LH_2$  target, that the recoil mass squared be in the neighborhood of the mass of the proton squared, that scattered particles not be near the boundary of counter *V* at the third focus, and that the outgoing trajectory not pass through any inefficient regions of PWC station 4. (These inefficient regions were included in the Monte Carlo simulation discussed below.)

The cut on the scatter vertex position eliminated a large fraction of the events because the trigger accepted scatters originating from the high-resolution PWC's immediately upstream and downstream of the target. These events, however, were clearly resolved from those originating in the target as evidenced by the almost negligible target-empty subtraction. The overall fraction of events that passed all the cuts was larger for the  $\pi^+$  and  $p$  data than for the  $\pi^-$  data. The  $\pi^+$  and  $p$  data were taken simultaneously, while the  $\pi^-$  data had different beam conditions during a separate running period.

At this point the normalized data was corrected for the acceptance of the apparatus. A Monte Carlo program calculated the acceptance as a function of  $q$ . Events were generated with the scattering vertex in the  $LH_2$  target and a flat distribution in  $q$ , and then traced through the apparatus. The incident-beam phase space was derived from actual incoming beam tracks. Multiple scattering of the particle was simulated at the appro-

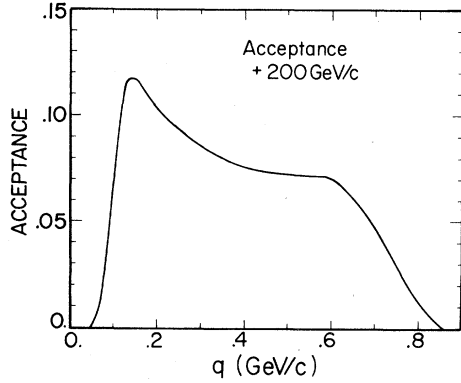


FIG. 4. Apparatus acceptance for  $\pi^+p$  and  $pp$  at 200 GeV/c.

appropriate places, and local PWC inefficiencies and the effects of resolution on the application of the cuts to the kinematic quantities were taken into account.

The geometric acceptance for the  $\pi^+p$  and  $pp$  data is shown in Fig. 4. The acceptance is particle independent for data taken at the same time. The acceptance for the  $\pi^-p$  data is similar in shape.

There were two effects not included in the Monte Carlo calculation: (1) radiative effects, and (2) contamination of the elastic signal by inelastic scatters. Both of these processes lead to  $t$ -dependent corrections to the scattering distributions since they change the shape of the recoil-mass-squared distribution in a  $t$ -dependent manner.

Using Sogard's<sup>10</sup> formalism for radiative corrections and taking into account the apparatus resolution, we calculated the correction for our cut on recoil mass squared. The measured differential cross section is corrected as follows:

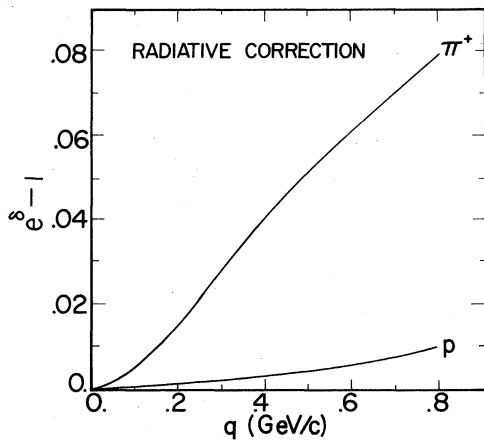


FIG. 5. Correction for radiative effects. The data are corrected by  $e^\delta$  (as explained in text).

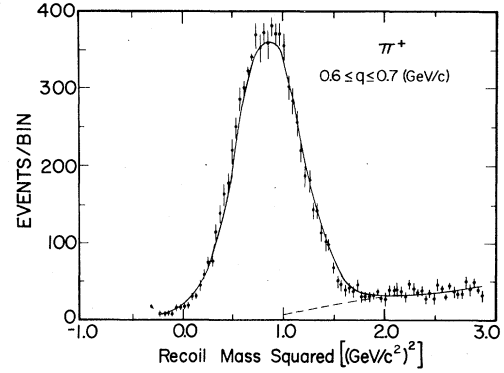


FIG. 6. Result of a fit (solid line) used to calculate the amount of inelastic contamination. The specific case is for  $\pi^+p$  scattering for  $0.06 \leq q \leq 0.07$  GeV/c. The dashed line is the inelastic contribution from the fit.

$$\left(\frac{d\sigma}{dt}\right)_{\text{corrected}} = e^\delta \left(\frac{d\sigma}{dt}\right)_{\text{measured}}, \quad (5)$$

where Fig. 5 presents  $(e^\delta - 1)$ . The  $\pi^-$  correction is identical to that for the  $\pi^+$  to one part in  $10^4$ .

The correction due to inelastic scatters was found by fitting the recoil-mass-squared distribution associated with different bins of  $q$  to an elastic peak and a term representing the inelastic scattering contribution. Figure 6 presents the results of one such fit. The amount of contamination was derived for our recoil-mass-squared cut. The percentage of inelastic contamination as a function of  $q$  is given in Fig. 7; it is approximately 2% at the smallest scattering angles and increases to 6% for pions and to 9% for the protons at the larger angles. The error on this correction is 10% of its magnitude. The measured differential cross section is corrected for the inelastic contamination as follows:

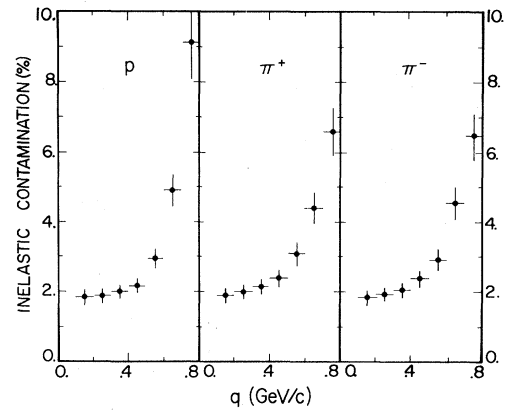


FIG. 7. Inelastic contamination. The data are corrected as indicated in the text.

$$\left(\frac{d\sigma}{dt}\right)_{\text{corrected}} = (1 - \alpha) \left(\frac{d\sigma}{dt}\right)_{\text{measured}}, \quad (6)$$

where  $\alpha$  is the inelastic contamination.

We found that our final results are not very sensitive to these two corrections. Each applied separately causes the extracted local slopes (see the next section) to vary by less than one standard deviation. Note that these two corrections act in opposite directions.

The final correction applied to the data was to correct for plural nuclear scattering (double scattering) in the hydrogen target. A particle may scatter twice before exiting the hydrogen target. These two small-angle scatters can simulate a large-angle scatter and thus artificially increase the cross section at large  $t$ . Hence if a correction for this effect is not made, one will measure for the single-scattering distribution a shallower slope than the actual slope.

To make the correction, the data was multiplied by  $P_s$  where

$$P_s = 1 + \frac{k}{b} e^{(bt-ct)/2}, \quad (7)$$

where  $t < 0$  and

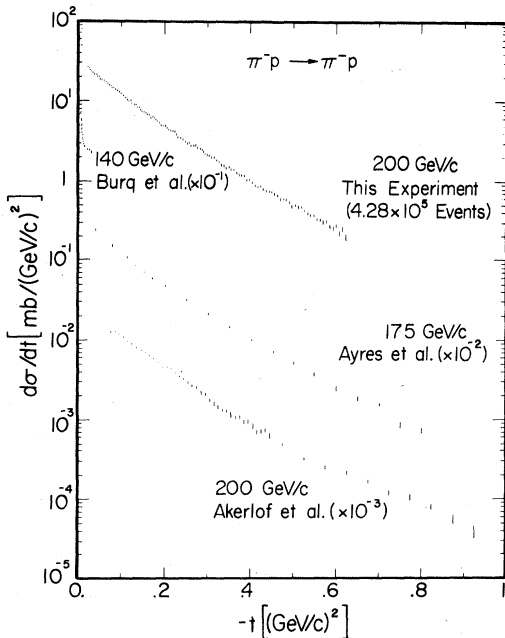


FIG. 8.  $d\sigma/dt$  for  $\pi^-p$  elastic scattering as measured by this experiment (corrected for Coulomb-scattering contributions, radiative effects, inelastic contamination, and plural nuclear scattering in the hydrogen target). Also shown are results from selected experiments which have been multiplied by the indicated powers of 10 for plotting. The data of Burq *et al.* (Ref. 6) include Coulomb scattering.

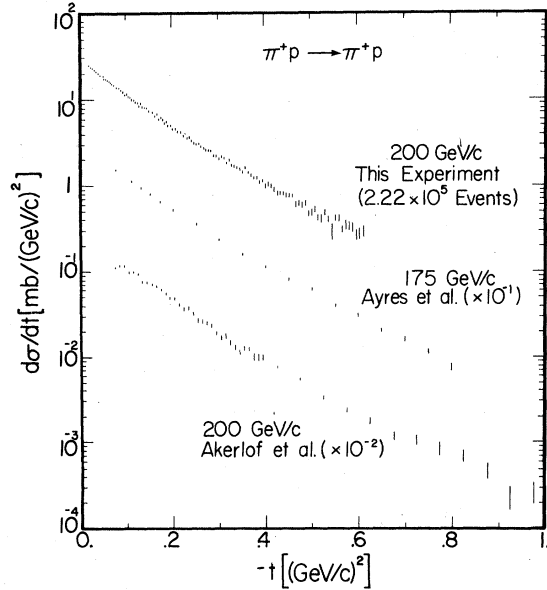


FIG. 9.  $d\sigma/dt$  for  $\pi^+p$  elastic scattering as measured by this experiment (corrected for Coulomb-scattering contributions, radiative effects, inelastic contamination, and plural nuclear scattering in the hydrogen target). Also shown are results from selected experiments multiplied by the indicated powers of 10.

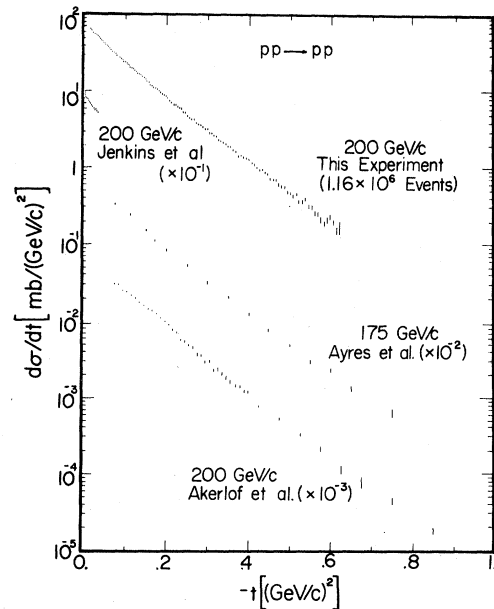


FIG. 10.  $d\sigma/dt$  for elastic  $pp$  scattering as measured by this experiment (corrected for Coulomb-scattering contributions, radiative effects, inelastic contamination, and plural nuclear scattering in the hydrogen target). Also shown are results from selected experiments, multiplied by the indicated powers of 10. The data of Jenkins *et al.* (Ref. 11) include Coulomb scattering.

TABLE II. Tabulation of differential cross sections. Errors are statistical only. Coulomb-scattering contributions have been subtracted, and corrections for radiative effects, inelastic contamination, and plural nuclear scattering are included.

$-t$ [(GeV/c) <sup>2</sup> ]	$d\sigma/dt$ [mb/(GeV/c) <sup>2</sup> ]	$-t$ [(GeV/c) <sup>2</sup> ]	$d\sigma/dt$ [mb/(GeV/c) <sup>2</sup> ]
$\pi^-p$ 200 GeV/c		$\pi^-p$ 200 GeV/c	
0.0206	25.28 ± 0.47	0.1857	5.33 ± 0.12
0.0221	24.43 ± 0.47	0.1901	5.04 ± 0.12
0.0236	24.24 ± 0.45	0.1945	4.81 ± 0.12
0.0252	24.08 ± 0.44	0.1990	4.85 ± 0.12
0.0268	23.81 ± 0.43	0.2035	4.59 ± 0.11
0.0285	22.61 ± 0.41	0.2081	4.38 ± 0.10
0.0302	22.49 ± 0.41	0.2127	4.29 ± 0.11
0.0320	21.65 ± 0.39	0.2173	4.18 ± 0.11
0.0338	21.72 ± 0.38	0.2221	4.10 ± 0.10
0.0357	21.67 ± 0.39	0.2268	3.85 ± 0.10
0.0377	20.47 ± 0.36	0.2317	3.50 ± 0.09
0.0396	19.62 ± 0.35	0.2366	3.52 ± 0.10
0.0417	20.50 ± 0.37	0.2415	3.43 ± 0.09
0.0438	19.68 ± 0.36	0.2465	3.14 ± 0.09
0.0459	19.02 ± 0.34	0.2515	2.99 ± 0.08
0.0481	19.03 ± 0.35	0.2566	3.05 ± 0.08
0.0503	18.70 ± 0.34	0.2617	2.84 ± 0.08
0.0526	18.40 ± 0.33	0.2669	2.78 ± 0.08
0.0549	18.03 ± 0.34	0.2721	2.79 ± 0.08
0.0573	17.44 ± 0.33	0.2773	2.57 ± 0.08
0.0598	16.78 ± 0.31	0.2827	2.56 ± 0.07
0.0622	16.38 ± 0.30	0.2881	2.47 ± 0.07
0.0648	15.89 ± 0.30	0.2936	2.21 ± 0.07
0.0674	15.65 ± 0.30	0.2990	2.09 ± 0.06
0.0700	15.51 ± 0.29	0.3046	2.10 ± 0.06
0.0727	14.83 ± 0.29	0.3102	1.95 ± 0.06
0.0755	14.77 ± 0.28	0.3158	1.95 ± 0.06
0.0782	14.35 ± 0.27	0.3215	1.82 ± 0.06
0.0811	14.21 ± 0.27	0.3272	1.73 ± 0.06
0.0840	12.96 ± 0.25	0.3330	1.52 ± 0.05
0.0869	13.97 ± 0.27	0.3389	1.52 ± 0.05
0.0899	12.28 ± 0.24	0.3448	1.46 ± 0.05
0.0930	12.87 ± 0.25	0.3507	1.56 ± 0.05
0.0961	11.99 ± 0.23	0.3567	1.40 ± 0.05
0.0992	11.71 ± 0.24	0.3627	1.40 ± 0.05
0.1024	10.98 ± 0.22	0.3688	1.28 ± 0.04
0.1057	11.00 ± 0.23	0.3750	1.21 ± 0.04
0.1090	10.45 ± 0.21	0.3812	1.18 ± 0.04
0.1123	10.07 ± 0.21	0.3874	1.16 ± 0.04
0.1157	10.02 ± 0.21	0.3937	1.02 ± 0.04
0.1192	9.42 ± 0.20	0.4001	1.04 ± 0.04
0.1227	9.05 ± 0.19	0.4065	0.95 ± 0.04
0.1263	9.33 ± 0.20	0.4129	0.89 ± 0.04
0.1299	8.97 ± 0.19	0.4194	0.85 ± 0.04
0.1335	8.58 ± 0.18	0.4260	0.85 ± 0.04
0.1372	8.39 ± 0.18	0.4326	0.71 ± 0.04
0.1410	7.78 ± 0.17	0.4393	0.73 ± 0.03
0.1448	7.48 ± 0.17	0.4460	0.74 ± 0.03
0.1487	7.38 ± 0.16	0.4527	0.72 ± 0.03
0.1526	7.07 ± 0.16	0.4595	0.69 ± 0.03
0.1565	6.77 ± 0.15	0.4664	0.66 ± 0.03
0.1605	6.61 ± 0.14	0.4733	0.58 ± 0.03
0.1646	6.18 ± 0.14	0.4803	0.58 ± 0.03
0.1687	6.12 ± 0.13	0.4873	0.57 ± 0.03
0.1729	6.14 ± 0.14	0.4943	0.53 ± 0.03
0.1771	5.90 ± 0.13	0.5014	0.46 ± 0.03
0.1814	5.70 ± 0.13	0.5086	0.48 ± 0.03

TABLE II. (Continued.)

$-t$ [(GeV/c) <sup>2</sup> ]	$d\sigma/dt$ [mb/(GeV/c) <sup>2</sup> ]	$-t$ [(GeV/c) <sup>2</sup> ]	$d\sigma/dt$ [mb/(GeV/c) <sup>2</sup> ]
$\pi^-p$ 200 GeV/c		$\pi^-p$ 200 GeV/c	
0.5158	0.47 ± 0.03	0.5908	0.27 ± 0.02
0.5231	0.46 ± 0.03	0.5985	0.25 ± 0.02
0.5304	0.42 ± 0.02	0.6063	0.27 ± 0.02
0.5378	0.38 ± 0.03	0.6142	0.22 ± 0.03
0.5452	0.36 ± 0.02	0.6221	0.24 ± 0.02
0.5526	0.35 ± 0.02	0.6301	0.19 ± 0.02
0.5602	0.33 ± 0.02	0.6382	0.23 ± 0.03
0.5677	0.32 ± 0.02	0.6462	0.21 ± 0.02
0.5754	0.31 ± 0.02	0.6544	0.21 ± 0.02
0.5830	0.31 ± 0.02	0.6625	0.19 ± 0.02
$\pi^+p$ 200 GeV/c		$\pi^+p$ 200 GeV/c	
0.0220	24.01 ± 0.46	0.1442	7.66 ± 0.18
0.0235	23.44 ± 0.42	0.1481	7.10 ± 0.17
0.0251	23.52 ± 0.44	0.1520	7.19 ± 0.18
0.0267	23.13 ± 0.42	0.1559	6.91 ± 0.17
0.0284	22.82 ± 0.40	0.1599	6.96 ± 0.16
0.0301	22.23 ± 0.40	0.1640	6.33 ± 0.16
0.0319	21.69 ± 0.39	0.1681	6.52 ± 0.16
0.0337	21.93 ± 0.39	0.1722	5.77 ± 0.15
0.0356	20.81 ± 0.38	0.1764	5.89 ± 0.15
0.0375	20.57 ± 0.37	0.1807	5.69 ± 0.14
0.0395	20.45 ± 0.36	0.1850	5.17 ± 0.14
0.0415	19.90 ± 0.35	0.1893	5.30 ± 0.15
0.0436	19.14 ± 0.35	0.1937	4.86 ± 0.14
0.0457	18.63 ± 0.34	0.1982	4.86 ± 0.14
0.0479	18.68 ± 0.33	0.2027	4.37 ± 0.12
0.0501	18.15 ± 0.34	0.2072	4.33 ± 0.13
0.0524	17.22 ± 0.32	0.2118	4.33 ± 0.13
0.0547	17.11 ± 0.31	0.2165	4.07 ± 0.12
0.0571	16.79 ± 0.31	0.2212	3.96 ± 0.11
0.0595	16.46 ± 0.30	0.2259	3.64 ± 0.11
0.0620	16.24 ± 0.30	0.2308	3.84 ± 0.11
0.0645	16.16 ± 0.29	0.2356	3.40 ± 0.11
0.0671	15.54 ± 0.29	0.2405	3.41 ± 0.11
0.0697	15.06 ± 0.28	0.2455	3.18 ± 0.10
0.0724	14.73 ± 0.28	0.2505	2.99 ± 0.10
0.0752	14.37 ± 0.27	0.2556	2.93 ± 0.10
0.0779	13.65 ± 0.26	0.2607	2.98 ± 0.10
0.0808	13.50 ± 0.26	0.2658	2.77 ± 0.09
0.0837	12.96 ± 0.25	0.2710	2.62 ± 0.09
0.0866	13.29 ± 0.26	0.2763	2.51 ± 0.09
0.0896	12.57 ± 0.25	0.2816	2.49 ± 0.09
0.0926	12.14 ± 0.24	0.2870	2.40 ± 0.08
0.0957	11.89 ± 0.24	0.2924	2.15 ± 0.08
0.0988	11.15 ± 0.24	0.2979	2.11 ± 0.08
0.1020	11.29 ± 0.23	0.3034	1.98 ± 0.08
0.1053	10.75 ± 0.23	0.3089	2.05 ± 0.07
0.1086	10.63 ± 0.22	0.3146	2.00 ± 0.07
0.1119	9.97 ± 0.21	0.3202	1.74 ± 0.07
0.1153	9.93 ± 0.21	0.3259	1.85 ± 0.07
0.1187	9.57 ± 0.21	0.3317	1.65 ± 0.06
0.1222	9.17 ± 0.21	0.3375	1.57 ± 0.06
0.1258	8.95 ± 0.20	0.3434	1.55 ± 0.07
0.1293	8.48 ± 0.19	0.3493	1.47 ± 0.07
0.1330	8.80 ± 0.19	0.3553	1.36 ± 0.06
0.1367	8.06 ± 0.18	0.3613	1.51 ± 0.06
0.1404	7.91 ± 0.18	0.3674	1.34 ± 0.06

TABLE II. (Continued.)

$-t$ [(GeV/c) <sup>2</sup> ]	$d\sigma/dt$ [mb/(GeV/c) <sup>2</sup> ]	$-t$ [(GeV/c) <sup>2</sup> ]	$d\sigma/dt$ [mb/(GeV/c) <sup>2</sup> ]
$\pi^+p$ 200 GeV/c		$\pi^+p$ 200 GeV/c	
0.3735	1.24 ± 0.06	0.5066	0.47 ± 0.05
0.3797	1.15 ± 0.05	0.5138	0.49 ± 0.04
0.3859	1.13 ± 0.05	0.5210	0.40 ± 0.04
0.3922	1.03 ± 0.06	0.5283	0.39 ± 0.05
0.3985	1.06 ± 0.06	0.5356	0.44 ± 0.04
0.4049	0.94 ± 0.06	0.5430	0.37 ± 0.04
0.4113	0.97 ± 0.06	0.5505	0.27 ± 0.06
0.4178	0.92 ± 0.06	0.5579	0.39 ± 0.04
0.4243	0.84 ± 0.06	0.5655	0.39 ± 0.04
0.4309	0.77 ± 0.04	0.5731	0.29 ± 0.04
0.4375	0.76 ± 0.04	0.5807	0.33 ± 0.04
0.4442	0.75 ± 0.04	0.5884	0.32 ± 0.04
0.4509	0.73 ± 0.04	0.5962	0.30 ± 0.04
0.4577	0.72 ± 0.04	0.6039	0.25 ± 0.04
0.4645	0.71 ± 0.04	0.6118	0.26 ± 0.04
0.4714	0.57 ± 0.05	0.6197	0.27 ± 0.04
0.4784	0.58 ± 0.04	0.6276	0.13 ± 0.08
0.4853	0.55 ± 0.04	0.6356	0.21 ± 0.04
0.4924	0.58 ± 0.04	0.6437	0.18 ± 0.04
0.4995	0.45 ± 0.04	0.6518	0.17 ± 0.04
		0.6599	0.15 ± 0.04
$pp$ 200 GeV/c		$pp$ 200 GeV/c	
0.0206	61.82 ± 0.60	0.1020	24.21 ± 0.28
0.0220	60.85 ± 0.58	0.1053	23.43 ± 0.27
0.0235	59.02 ± 0.56	0.1086	22.26 ± 0.26
0.0251	58.31 ± 0.56	0.1119	21.88 ± 0.26
0.0267	57.68 ± 0.55	0.1153	20.40 ± 0.25
0.0284	56.52 ± 0.55	0.1187	19.82 ± 0.24
0.0301	55.31 ± 0.53	0.1222	19.28 ± 0.23
0.0319	54.34 ± 0.53	0.1258	18.25 ± 0.22
0.0337	52.80 ± 0.51	0.1293	17.61 ± 0.22
0.0356	52.02 ± 0.50	0.1330	16.83 ± 0.21
0.0375	51.08 ± 0.50	0.1367	16.37 ± 0.20
0.0395	49.16 ± 0.48	0.1404	15.88 ± 0.20
0.0415	48.09 ± 0.47	0.1442	15.27 ± 0.20
0.0436	46.67 ± 0.46	0.1481	14.67 ± 0.19
0.0457	46.17 ± 0.46	0.1520	14.25 ± 0.19
0.0479	45.02 ± 0.45	0.1559	13.25 ± 0.18
0.0501	43.28 ± 0.43	0.1599	12.80 ± 0.17
0.0524	41.85 ± 0.42	0.1640	11.96 ± 0.16
0.0547	40.98 ± 0.41	0.1681	11.71 ± 0.16
0.0571	40.05 ± 0.40	0.1722	11.11 ± 0.16
0.0595	38.99 ± 0.40	0.1764	10.70 ± 0.15
0.0620	38.17 ± 0.39	0.1807	10.28 ± 0.15
0.0645	36.46 ± 0.38	0.1850	9.82 ± 0.14
0.0671	35.48 ± 0.37	0.1893	9.50 ± 0.14
0.0697	34.73 ± 0.37	0.1937	8.83 ± 0.13
0.0724	33.22 ± 0.35	0.1982	8.60 ± 0.13
0.0752	32.26 ± 0.34	0.2027	8.29 ± 0.12
0.0779	31.34 ± 0.34	0.2072	7.94 ± 0.12
0.0808	30.23 ± 0.33	0.2118	7.35 ± 0.11
0.0837	29.21 ± 0.32	0.2165	7.00 ± 0.11
0.0866	29.24 ± 0.32	0.2212	6.48 ± 0.10
0.0896	27.59 ± 0.30	0.2259	6.40 ± 0.10
0.0926	26.45 ± 0.29	0.2308	6.07 ± 0.10
0.0957	25.77 ± 0.29	0.2356	5.81 ± 0.10
0.0988	24.40 ± 0.28	0.2405	5.68 ± 0.09

TABLE II. (Continued.)

$-t$ [(GeV/c) <sup>2</sup> ]	$d\sigma/dt$ [mb/(GeV/c) <sup>2</sup> ]	$-t$ [(GeV/c) <sup>2</sup> ]	$d\sigma/dt$ [mb/(GeV/c) <sup>2</sup> ]
$pp$ 200 GeV/c		$pp$ 200 GeV/c	
0.2455	5.23 ± 0.09	0.4309	0.86 ± 0.03
0.2505	5.03 ± 0.09	0.4375	0.85 ± 0.03
0.2556	4.61 ± 0.08	0.4442	0.79 ± 0.03
0.2607	4.34 ± 0.08	0.4509	0.76 ± 0.03
0.2658	4.21 ± 0.08	0.4577	0.64 ± 0.03
0.2710	4.14 ± 0.08	0.4645	0.63 ± 0.03
0.2763	3.66 ± 0.07	0.4714	0.62 ± 0.03
0.2816	3.57 ± 0.07	0.4784	0.54 ± 0.02
0.2870	3.53 ± 0.07	0.4853	0.51 ± 0.02
0.2924	3.28 ± 0.06	0.4924	0.49 ± 0.02
0.2979	3.06 ± 0.06	0.4995	0.44 ± 0.02
0.3034	3.06 ± 0.06	0.5066	0.42 ± 0.02
0.3089	2.73 ± 0.06	0.5138	0.38 ± 0.02
0.3146	2.67 ± 0.06	0.5210	0.40 ± 0.02
0.3202	2.50 ± 0.05	0.5283	0.32 ± 0.02
0.3259	2.44 ± 0.05	0.5356	0.32 ± 0.02
0.3317	2.21 ± 0.05	0.5430	0.34 ± 0.02
0.3375	2.13 ± 0.05	0.5505	0.28 ± 0.02
0.3434	2.02 ± 0.05	0.5579	0.27 ± 0.02
0.3493	1.90 ± 0.05	0.5655	0.23 ± 0.02
0.3553	1.77 ± 0.04	0.5731	0.21 ± 0.02
0.3613	1.76 ± 0.04	0.5807	0.18 ± 0.02
0.3674	1.61 ± 0.04	0.5884	0.16 ± 0.02
0.3735	1.53 ± 0.04	0.5962	0.19 ± 0.02
0.3797	1.31 ± 0.04	0.6039	0.20 ± 0.02
0.3859	1.32 ± 0.04	0.6118	0.17 ± 0.02
0.3922	1.27 ± 0.04	0.6197	0.13 ± 0.02
0.3985	1.23 ± 0.04	0.6276	0.14 ± 0.03
0.4049	1.17 ± 0.03	0.6356	0.11 ± 0.03
0.4113	1.04 ± 0.03	0.6437	0.10 ± 0.02
0.4178	1.01 ± 0.03	0.6518	0.11 ± 0.02
0.4243	0.91 ± 0.03	0.6599	0.10 ± 0.02

$$b = b(t=0) = 9.89, 9.93, \text{ and } 11.74 \text{ (GeV/c)}^{-2}$$

for  $\pi^-p$ ,  $\pi^+p$ , and  $pp$ ,

$$c = 3.47, 3.72, \text{ and } 3.16 \text{ (GeV/c)}^{-4}$$

for  $\pi^-p$ ,  $\pi^+p$ , and  $pp$ ,

$$k = \Gamma\sigma_t^2/64\pi\hbar^2,$$

$\sigma_t$  = hadron-proton total cross section,

$$\Gamma = N_A \rho x / A,$$

$N_A$  = Avogadro's number,

$\rho$  = target density,

$x$  = target length,

$A$  = atomic weight of hydrogen.

These values of  $b$  and  $c$  are the results of fits to the data that will be discussed in detail below.

At  $-t = 0.1, 0.4, \text{ and } 0.6, \text{ (GeV/c)}^2$  this correction is 0.3%, 1.4%, and 4.2%, respectively, for  $\pi^\pm p$  elastic scattering and 0.7%, 4%, and 14%, re-

spectively, for  $pp$  elastic scattering. The fractional uncertainty in the correction is 5%.

## RESULTS

The  $d\sigma/dt$  distribution is calculated using the following formula:

$$\frac{d\sigma}{dt} = \frac{N_s(q)e^\delta(1-\alpha)P_s}{2q\Gamma\epsilon(q)\Delta}, \quad (8)$$

where

$N_s(q)$  = normalized number of scattered particles in each  $q$  bin that pass all cuts,

$\epsilon(q)$  = acceptance as function of  $q$ ,

$\Delta = q$  bin size,

$P_s, \delta, \alpha$  = correction parameters as defined in Eqs. (5), (6), and (7).

Figures 8 to 10 show the resulting  $d\sigma/dt$  distributions for  $\pi^-p$ ,  $\pi^+p$ , and  $pp$  elastic scattering; Table II gives the numerical values of the cross section in units of  $\text{mb}/(\text{GeV/c})^2$ . The  $pp$ ,  $\pi^+p$ ,

and  $\pi^-p$  distributions contain  $1.16 \times 10^6$ ,  $2.22 \times 10^5$ , and  $4.28 \times 10^5$  events, respectively. The errors shown are statistical only; there is an uncertainty in the overall normalization of 4.0%. This uncertainty is due mainly to the statistical error involved in our method of counting the number of incident-beam particles. The data have not been corrected so as to extrapolate to the optical point.

By varying the cuts used to extract the elastic signal, we estimate the following  $t$ -dependent systematic error on the  $d\sigma/dt$  distributions:  $\pm 0.5\%$  for  $0.02 \leq -t \leq 0.20$  (GeV/c) $^2$ ,  $\pm 1\%$  for  $0.20 < -t \leq 0.35$  (GeV/c) $^2$ ,  $\pm 2\%$  for  $0.35 < -t \leq 0.50$  (GeV/c) $^2$ , and  $\pm 4\%$  for  $0.50 < -t \leq 0.67$  (GeV/c) $^2$ .

The displayed and tabulated  $d\sigma/dt$  distributions have been corrected for inelastic contamination, for radiative effects, and for plural nuclear scattering. Also the contribution due to Coulomb scattering (including the Coulomb-nuclear-interference contribution) has been removed. Table III presents the parameters used for this subtraction. The Coulomb correction is negligible above  $-t = 0.035$  (GeV/c) $^2$  and only slightly significant below. Making reasonable variations of the parameters listed in Table III changes the derived local slopes by less than one standard deviation.

Figures 8 to 10 show a comparison of the differential cross sections for some of the experiments<sup>2,3,6,11</sup> that have measured elastic scattering in the same kinematic region. Note that our data display high statistical accuracy and bridge a  $t$  range not covered by any other single experiment.

TABLE III. Parameters for Coulomb-scattering contribution to  $d\sigma/dt$ :

$$\left. \frac{d\sigma}{dt} \right|_{\text{Coulomb}}^{\pm} = \frac{4\pi\alpha^2}{\beta^2 t^2} \mp \sigma_{hp} e^{bt} / \alpha \rho / \beta t,$$

where  $\alpha$  = fine-structure constant,  $\rho$  = ratio of real to imaginary part of the scattering amplitude,  $\sigma_{hp}$  = total cross section for hadron-proton scattering,  $b$  = forward logarithmic nuclear slope, and  $\beta$  = particle velocity/c.

	$b$ [(GeV/c) $^{-2}$ ]	$\sigma_{hp}$ (mb) <sup>a</sup>	$\rho$ <sup>b</sup>
$p-p$	12.0	38.97	-0.01
$\pi^+-p$	10.5	23.84	0.04
$\pi^-p$	10.5	24.33	0.08

<sup>a</sup>From A. S. Carroll *et al.*, Phys. Rev. Lett. **33**, 928 (1974); **33**, 932 (1974).

<sup>b</sup>From R. D. Hendrick and B. Lautrup, Phys. Rev. **D 11**, 529 (1975).

### EXTRACTION OF THE LOCAL-SLOPE PARAMETERS

In order to study in detail the shape of the  $d\sigma/dt$  distribution, we fit over small regions of  $t$  using an exponential form. Thus in the limit of an infinitely-small- $t$  region, we obtain the forward slope  $b$  as a function of  $t$  using Eq. (3). To orient the reader, we present Fig. 11 which shows what might be expected in a  $b$  vs  $t$  plot for some simple functional forms of  $d\sigma/dt$ .

In the analysis we subdivided the entire  $t$  range into 9 or 10 subregions and still maintained small errors on the measured local slopes. The fits were performed using a least-squares minimization procedure; the program MINUIT<sup>12</sup> was employed. The fitting method was such that the values of  $d\sigma/dt$  at the end point of the  $i$ th subregion was constrained to coincide with that at the beginning point of the  $(i+1)$ th subregion. This, of course, introduced correlations between the measured local slopes. When fits were performed without the above constraint, the values of the local slopes were within a standard deviation of the results from the constrained fits. The constrained fits merely reduced the statistical errors of the results.

To estimate the systematic error,<sup>13</sup> we derived the local slopes varying in turn each of cuts 5 through 10 of Table I. For example, we changed the veto size, while keeping all other cuts the same. Our estimate of the systematic error on a particular local slope is the maximum range of the values of that local slope obtained with different sets of cuts. It should be noted that the systematic error includes all resolution-dependent effects introduced by cuts on kinematic quantities such as the scattering vertex position and the recoil mass squared.

Since the plural-scattering correction of Eq. (7)

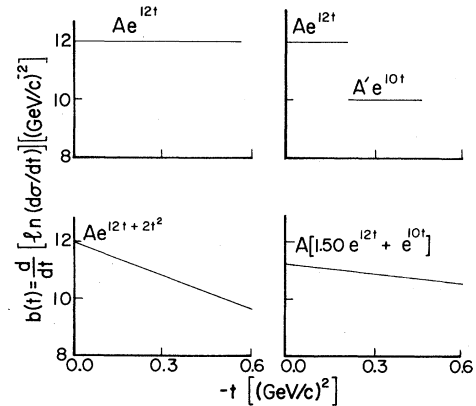


FIG. 11. Local slope as a function of  $t$  for some representative shapes of  $d\sigma/dt$ .

presupposes a slope and curvature, the fits were made to the data of Table II without this correction. Inclusion of this correction with reasonable variations of  $b$  and  $c$  make less than half a standard-deviation difference in the values of the local slopes.

Another source of systematic error was the  $\pm 1\%$  uncertainty in the absolute value of the incident-beam momentum. This contribution is included in the systematic errors presented in Table IV. Note that in some cases the total systematic error is significant when compared to the statistical error on the local slope.

We present in Fig. 12 and Table IV the results of this type of analysis. The errors shown in Fig. 12 include both the statistical and systematic contribution added in quadrature.

We also show on Fig. 12 the results of a fit of  $d\sigma/dt$  over the full  $t$  range to a quadratic form. Table V exhibits the values of  $b$  and  $c$  derived from these fits. In these fits, the plural scattering correction was included properly by fitting the uncorrected data to the form

$$\frac{d\sigma}{dt} = A e^{bt+ct^2} \left( 1 + \frac{k}{b} e^{(bt-ct^2)/2} \right),$$

where  $k$  is defined in Eq. (7).

#### DISCUSSION OF LOCAL SLOPES

The data presented in Fig. 12 clearly demonstrate that the elastic scattering differential cross sections for the  $\pi^\pm p$  and  $pp$  reactions at 200 GeV/ $c$  are not consistent with a simple exponential  $e^{bt}$ . For  $pp$  scattering the behavior is poorly parametrized by an exponential with a quadratic term  $e^{bt+ct^2}$  (see Table V). However, for  $\pi^\pm p$  scattering, this form describes the  $t$  distributions for  $-t \geq 0.04$  (GeV/ $c$ )<sup>2</sup>.

The local slope in the  $pp$  case decreases with increasing  $t$  in the region of  $0.03 < -t < 0.25$  (GeV/ $c$ )<sup>2</sup>. From  $0.25 < -t < 0.65$  (GeV/ $c$ )<sup>2</sup> the local slope has a constant value of approximately 9.5 (GeV/ $c$ )<sup>-2</sup>.

For the pions, in the region  $0.10 < -t < 0.60$  (GeV/ $c$ )<sup>2</sup> the local slope decreases with increasing  $t$ . From  $0.03 < -t < 0.10$  (GeV/ $c$ )<sup>2</sup> the local slope is relatively flat; finally there is a sharp increase in the value in the region  $0.02 < -t < 0.03$  (GeV/ $c$ )<sup>2</sup>.

Figure 12 suggests that in the region of  $0.25 \leq -t \leq 0.60$  (GeV/ $c$ )<sup>2</sup> the dependence of the local slopes as a function of  $t$  is different for protons and pions. While we believe our results suggest the above, the data do not have sufficient statistical accuracy to conclusively demonstrate this supposition. We formed the ratio  $R^\pm$  where

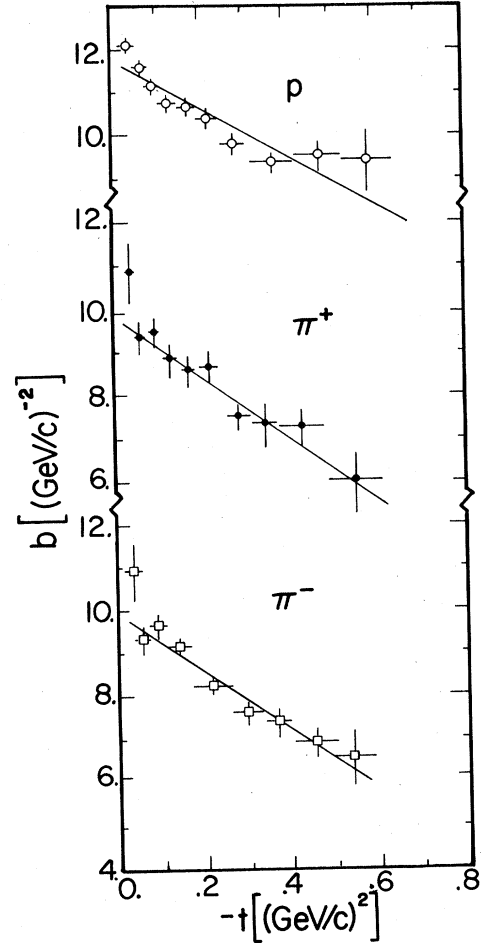


FIG. 12. Local slope as a function of  $t$  for  $\pi^-p$ ,  $\pi^+p$ , and  $pp$  elastic scattering. Errors include both statistical and systematic errors added in quadrature. Solid lines present local slope as calculated from fits of  $d\sigma/dt$  to  $\exp(bt+ct^2)$ .

$$R^\pm = \frac{(d\sigma/dt)(pp)}{(d\sigma/dt)(\pi^\pm p)} \quad (9)$$

and fit the ratio to the form  $Ce^{dt}$ . Table VI presents the fit results. An exponential describes the general behavior of  $R^\pm$  (for the  $\pi^-$  case there is no one region of  $-t$  that gives a large contribution to the  $\chi^2$ ) which would indicate similar  $d\sigma/dt$  shapes for the protons and pions. Also, the value of  $d$  is in good agreement with what was found at 175 GeV/ $c$  by Ref. 2. To definitively settle the question approximately four times our present statistics in the region of  $0.30 \leq -t \leq 0.60$  (GeV/ $c$ )<sup>2</sup> is required.

Figure 13 compares our measured local slopes with those measured by others.<sup>2,3,5,6,14,15</sup> It should be noted that these other measurements of the forward slopes are derived from fits over much

TABLE IV. Local-slope values and correlations.

Local slope	$t$   range [(GeV/c) <sup>2</sup> ]	$\pi^+p$ 200 GeV/c								
		Value <sup>a</sup> [(GeV/c) <sup>-2</sup> ]								
$b_1$	0.022–0.036	10.91 ± 0.55	(0.25)							
$b_2$	0.036–0.062	9.30 ± 0.29	(0.18)							
$b_3$	0.062–0.102	9.63 ± 0.23	(0.17)							
$b_4$	0.102–0.161	9.18 ± 0.17	(0.10)							
$b_5$	0.161–0.252	8.26 ± 0.11	(0.08)							
$b_6$	0.252–0.327	7.62 ± 0.16	(0.18)							
$b_7$	0.327–0.400	7.41 ± 0.24	(0.22)							
$b_8$	0.400–0.494	6.92 ± 0.27	(0.23)							
$b_9$	0.494–0.583	6.60 ± 0.49	(0.43)							
$\chi^2/\text{DOF} = \frac{130.4}{113}$										
Correlation coefficients <sup>b</sup> $\rho_{ij}$										
	$b_1$	$b_2$	$b_3$	$b_4$	$b_5$	$b_6$	$b_7$	$b_8$		
$b_2$		-0.499								
$b_3$		0.020	-0.511							
$b_4$		-0.102	0.391	-0.770						
$b_5$		0.231	-0.676	0.472	-0.591					
$b_6$		-0.238	0.674	-0.355	0.039	-0.388				
$b_7$		0.147	-0.413	0.200	0.058	-0.135	-0.507			
$b_8$		-0.067	0.187	-0.088	-0.037	0.110	0.016	-0.565		
$b_9$		0.024	-0.068	0.032	0.015	-0.045	0.018	0.116	-0.565	
$\chi^2/\text{DOF} = \frac{115.1}{116}$										
Correlation coefficients <sup>b</sup> $\rho_{ij}$										
	$b_1$	$b_2$	$b_3$	$b_4$	$b_5$	$b_6$	$b_7$	$b_8$	$b_9$	
$b_2$		0.211								
$b_3$		-0.454	-0.180							
$b_4$		-0.355	-0.644	0.110						
$b_5$		0.204	0.221	-0.316	-0.559					
$b_6$		0.036	0.044	-0.162	0.252	-0.675				
$b_7$		-0.160	-0.151	0.410	-0.287	0.232	-0.611			
$b_8$		0.141	0.131	-0.348	0.221	-0.103	0.126	-0.558		
$b_9$		-0.080	-0.075	0.198	-0.123	0.048	-0.027	0.122	-0.530	
$b_{10}$		0.032	0.030	-0.080	-0.049	-0.018	0.005	-0.021	0.109	-0.497

TABLE IV. (Continued.)

Local slope	$ t $ range [(GeV/c) <sup>2</sup> ]	$\pi^+p$ 200 GeV/c Value <sup>a</sup> [(GeV/c) <sup>-2</sup> ]
$b_1$	0.024–0.044	10.83 ± 0.63 (0.32)
$b_2$	0.044–0.072	9.33 ± 0.33 (0.19)
$b_3$	0.072–0.105	9.41 ± 0.31 (0.17)
$b_4$	0.105–0.144	8.83 ± 0.33 (0.18)
$b_5$	0.144–0.181	8.56 ± 0.33 (0.21)
$b_6$	0.181–0.241	8.64 ± 0.20 (0.30)
$b_7$	0.241–0.309	7.48 ± 0.24 (0.25)
$b_8$	0.309–0.374	7.26 ± 0.34 (0.34)
$b_9$	0.374–0.478	7.22 ± 0.30 (0.33)
$b_{10}$	0.478–0.604	5.96 ± 0.50 (0.42)

$\chi^2/\text{DOF} = \frac{39.1}{114}$

Correlation coefficients<sup>b</sup>  $\rho_{ij}$

	$b_1$	$b_2$	$b_3$	$b_4$	$b_5$	$b_6$	$b_7$	$b_8$	$b_9$
$b_2$	-0.673								
$b_3$	0.183	-0.503							
$b_4$	-0.029	0.182	-0.713						
$b_5$	-0.025	-0.379	0.533	-0.703					
$b_6$	0.046	0.476	-0.514	0.119	-0.382				
$b_7$	-0.030	-0.296	0.305	-0.003	-0.187	-0.404			
$b_8$	0.015	0.142	-0.145	-0.008	0.146	-0.065	-0.558		
$b_9$	-0.006	-0.054	0.055	0.004	-0.063	0.060	0.083	-0.582	
$b_{10}$	0.002	0.016	-0.017	-0.001	0.020	-0.022	-0.013	-0.124	-0.523

<sup>a</sup>Systematic error contribution in parentheses.

<sup>b</sup>The correlation coefficient  $\rho_{ij}$  is defined as  $\rho_{ij} \equiv C_{ij}/(\sigma_i\sigma_j)$ , where  $C_{ij}$  is the covariance between the quantities  $b_i$  and  $b_j$ , and  $\sigma_i$  is the standard deviation of  $b_i$ .

larger ranges of  $t$  than we used. This is especially true for Refs. 2 and 3, where fits to a quadratic form were performed over their full  $t$  range ( $-0.02$  to  $-0.40$  for Ref. 2;  $-0.07$  to  $-0.80$  for Ref. 3). From the fit results, the forward slope at  $t$  equal to  $-0.20$  (GeV/c)<sup>2</sup> is computed. We conclude that the quoted local slopes are in good agreement with our data.

To further investigate the agreement between our data and that of Refs. 2 and 3 we have compared the  $d\sigma/dt$  distributions directly. Interpolating between our two closest data points to the appropriate  $t$ , we formed the ratios  $RT(t)$ , dividing in turn the data of Refs. 2 and 3 by the data from

this experiment. We assume no  $s$  dependence between 175 and 200 GeV. These ratios were then fit to the form  $u - w|t|$ . The results of these fits are given in Table VII. The constant  $u$  reflects the relative normalization of the two data sets and a value of  $w$  different from zero or a poor  $\chi^2$  indicates a difference in shape. Inspection of Table VII shows that there is good agreement between our data and that of Ayres *et al.*,<sup>2</sup> particularly for  $pp$  scattering. The 3 to 5% normalization difference is consistent with the quoted 3% (Ref. 2) and the  $\pm 4\%$  normalization uncertainty in our data. The comparisons with the data of Ref. 3 have poor  $\chi^2$  which appear to be related to structure in the

TABLE V. Fits of  $d\sigma/dt$  to  $Ae^{bt+ct^2}$ .

	$ t $ range [(GeV/c) <sup>2</sup> ]	$A$ [mb/(GeV/c) <sup>2</sup> ]	$b$ [(GeV/c) <sup>-2</sup> ]	$c$ [(GeV/c) <sup>-4</sup> ]	$\chi^2/\text{DOF}$
$\pi^+p$	0.025–0.620	29.71 ± 0.17	9.93 ± 0.07	3.72 ± 0.16	$\frac{108.2}{125}$
$\pi^-p$	0.025–0.620	30.17 ± 0.16	9.89 ± 0.06	3.47 ± 0.12	$\frac{148.5}{125}$
$pp$	0.025–0.620	78.18 ± 0.24	11.74 ± 0.04	3.16 ± 0.09	$\frac{181}{125}$

TABLE VI. Results of fits of  $R^{\pm}$  (as defined in text) to  $Ce^{at}$ .

	$ t $ range [(GeV/c) <sup>2</sup> ]	C	d [(GeV/c) <sup>-2</sup> ]	$\chi^2/\text{DOF}$
$R^+(p/\pi^+)$	0.022–0.630	$2.67 \pm 0.01$	$2.08 \pm 0.06$	$\frac{126.1}{128}$
$R^-(p/\pi^-)$	0.022–0.630	$2.61 \pm 0.01$	$1.98 \pm 0.06$	$\frac{165.1}{128}$

data of Ref. 3. (See Figs. 8–10.)

Figure 13 clearly shows that the local slopes for  $\pi^+p$ ,  $\pi^-p$ , and  $pp$  elastic scattering are continuously increasing as  $|t|$  approaches zero. The results from Refs. 6 and 16 and the analysis of Ref. 17 support our observation of a sharp increase in the local slope for the very small  $t$

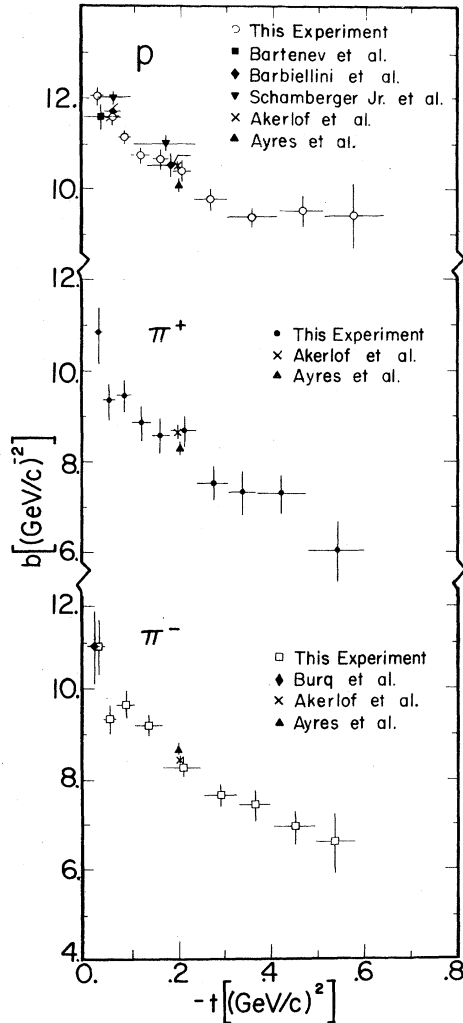


FIG. 13. Comparison of measurements by several experiments of the logarithmic slope for  $\pi^-p$ ,  $\pi^+p$ , and  $pp$  elastic scattering.

TABLE VII. Results from fits of  $RT(t)$  (as defined in text) to  $u-w|t|$ .

$ t $ range [(GeV/c) <sup>2</sup> ]	u	w [(GeV/c) <sup>-2</sup> ]	$\chi^2/\text{DOF}$
Comparison with Ref. 2(b)			
$pp$	$1.035 \pm 0.018$	$0.036 \pm 0.069$	1.09
$\pi^+p$	$1.032 \pm 0.018$	$-0.210 \pm 0.092$	1.02
$\pi^-p$	$1.052 \pm 0.018$	$0.109 \pm 0.070$	1.45
Comparison with Ref. 3			
$pp$	$1.047 \pm 0.013$	$0.229 \pm 0.063$	3.59
$\pi^+p$	$0.942 \pm 0.017$	$0.046 \pm 0.081$	2.84
$\pi^-p$	$1.011 \pm 0.013$	$0.319 \pm 0.056$	2.24

range in  $\pi^-p$  scattering. Figure 2 of Ref. 17 indicates that the behavior of the local slopes seen in Fig. 13 for  $\pi^-p$  scattering at 200 GeV/c is almost identical to the behavior at 100 GeV/c.

An analysis similar to ours has been performed for hadron-proton elastic scattering at energies of 10.4 and 14 GeV.<sup>4</sup> It was found that the  $\pi^+p$  and  $pp$  scattering exhibit a behavior more complicated than a simple exponential in  $t$ .

#### TOTAL ELASTIC CROSS SECTIONS

By integrating the  $d\sigma/dt$  measurements over  $t$ , we compute the total elastic cross sections. To calculate the contributions of the regions in  $t$  we did not directly measure, we used the results of the fits from which the local slopes were obtained. We found that when we extrapolated the  $d\sigma/dt$  distributions to  $t=0$ , we were consistent within our experimental errors with the optical point. For this extrapolation we used the fits of Table V. Therefore, we normalized  $d\sigma/dt$  to the optical point using the  $A$ 's from Table V when we calculated the total elastic cross sections. Table VIII presents the total elastic cross sections and the ratio of the total elastic cross section to the total cross section. The errors in Table VIII include, in addition to the statistical uncertainties, the systematic uncertainties due to our extrapolation

TABLE VIII. Total elastic cross sections at 200 GeV/c.

	$\sigma_e$ (mb)	$(\sigma_e/\sigma_t)^a$
$\pi^-p$	$3.32 \pm 0.15$	$0.136 \pm 0.006$
$\pi^+p$	$3.17 \pm 0.06$	$0.133 \pm 0.003$
$pp$	$6.87 \pm 0.13$	$0.176 \pm 0.004$

<sup>a</sup>Value of  $\sigma_t$  from A. S. Carroll *et al.*, Phys. Rev. Lett. **33**, 928 (1974); **33**, 932 (1974).

TABLE IX. Results of fits of  $d\sigma/dt$  to the form-factor parametrization with a quadratic matrix element, Eqs. (10) and (11a).

	$ t $ range (GeV/c) <sup>2</sup>	$A$ [mb/(GeV/c) <sup>2</sup> ]	$u$ [(GeV/c) <sup>-2</sup> ]	$r_\pi$ (fm)	$r_p$ (fm)	$\chi^2/\text{DOF}$
$pp$	0.025–0.620	79.32 ± 0.26	1.65 ± 0.03		0.79 ± 0.01	$\frac{124.9}{122}$
$\pi^+p$	0.025–0.620	30.27 ± 0.19	1.01 ± 0.08	0.61 ± 0.05	0.86 ± 0.04	$\frac{103.0}{122}$
$\pi^-p$	0.025–0.620	30.88 ± 0.18	1.09 ± 0.07	0.65 ± 0.04	0.82 ± 0.03	$\frac{136.1}{122}$

of the measured  $d\sigma/dt$  distributions over unmeasured  $t$  regions. Our results are in good agreement with Akerlof *et al.*<sup>3</sup> but in poor agreement with the statistically more precise data of Ayres *et al.*<sup>2</sup>

#### COMPARISONS OF THE DATA WITH THEORETICAL MODELS

Theoretical models such as those of Chou and Yang<sup>18</sup> and versions of the AQM (Refs. 19 and 20) attribute the major part of the small- $t$  elastic-cross-section variation to the hadronic form factors of the target and the projectile. These form factors are assumed to be the same as the electromagnetic form factors. In the AQM the form factors describe the spatial distribution of the clothed quarks; in the very-small- $t$  region, the scattering is dominated by single quark-quark scattering. In both these models the differential elastic cross section is given to first order as

$$\frac{d\sigma}{dt} = A F_t^2(t) F_p^2(t) |A_{qq}(t)|^2, \quad (10)$$

where

$$A = N_0 \sigma_t^2 / 16\pi \hbar^2,$$

$N_0$  = normalization factor,

$\sigma_t$  = total cross section,

$F_t(t)$  = hadronic form factor of the target,

$F_p(t)$  = hadronic form factor of the projectile,

$A_{qq}(t)$  = quark-quark-scattering matrix element.

In our analysis we assume the conventional dipole form for the proton form factor and the single-pole form for the pion:

$$F_p(t) = (1 - r_p^2 t / 12\hbar^2)^{-2},$$

$$F_\pi(t) = (1 - r_\pi^2 t / 6\hbar^2)^{-1},$$

where

$r_p$  = proton electromagnetic charge radius,

$r_\pi$  = pion electromagnetic charge radius.

We have fit our  $d\sigma/dt$  distributions to Eq. (10) using the following two forms for  $A_{qq}(t)$ :

$$|A_{qq}(t)|^2 = (1 + ut/2)^2, \quad \text{quadratic form,} \quad (11a)$$

$$|A_{qq}(t)|^2 = \exp(ut), \quad \text{exponential form.} \quad (11b)$$

The quadratic form is purely phenomenological; the exponential form is suggested by Bialas *et al.*<sup>20</sup> and Levin and Shekhter.<sup>20</sup> For the case of the exponential form [Eq. (11b)] one can identify  $u$  with the quark radius  $r_q$  where<sup>21</sup>

$$r_q^2 = -2\hbar^2 u. \quad (12)$$

Note that in the Chou-Yang model,  $A_{qq}(t)$  is unity. The results of the fits are given in Tables IX and X. In some cases the fitted parameters are highly correlated.

The data are well represented over the full  $t$  range [0.025 <  $-t$  < 0.620 (GeV/c)<sup>2</sup>] by Eq. (10) with the quadratic form for the quark-quark scattering matrix element [Eq. (11a)]. The fitted values of

TABLE X. Results of fits of  $d\sigma/dt$  to the form-factor parametrization with an exponential matrix element, Eqs. (10), (11b), and (12).

	$ t $ range [(GeV/c) <sup>2</sup> ]	$A$ [mb/(GeV/c) <sup>2</sup> ]	$r_q$ (fm)	$r_\pi$ (fm)	$r_p$ (fm)	$\chi^2/\text{DOF}$
$pp$	0.025–0.620	78.40 ± 0.27	0.51 ± 0.01		0.71 ± 0.01	$\frac{154.0}{122}$
$pp$	0.025–0.320	79.27 ± 0.36	0.46 ± 0.02		0.75 ± 0.01	$\frac{78.4}{78}$
$\pi^+p$	0.025–0.620	30.18 ± 0.21	0.34 ± 0.02	0.65 ± 0.04	0.79 ± 0.04	$\frac{103.0}{122}$
$\pi^+p$	0.025–0.320	30.11 ± 0.26	0.36 ± 0.04	0.63 ± 0.04	0.78 ± 0.04	$\frac{67.5}{78}$
$\pi^-p$	0.025–0.620	30.78 ± 0.19	0.40 ± 0.02	0.70 ± 0.03	0.72 ± 0.03	$\frac{136.0}{122}$
$\pi^-p$	0.025–0.320	30.91 ± 0.37	0.31 ± 0.06	0.61 ± 0.06	0.84 ± 0.04	$\frac{97.2}{78}$

TABLE XI. Results of fits of  $d\sigma/dt$  to form-factor parametrization using  $\pi^-p$ ,  $\pi^+p$ ,  $pp$  data simultaneously:  $|A_{qq}|^2 = \exp(-r_q^2/2\tilde{t}^2)$ .

$ t $ range [(GeV/c) <sup>2</sup> ]	$A_{\pi^-}$ [mb/(GeV/c) <sup>2</sup> ]	$A_{\pi^+}$ [mb/(GeV/c) <sup>2</sup> ]	$A_p$ [mb/(GeV/c) <sup>2</sup> ]	$r_q^{\pi^-}$ (fm)	$r_q^{\pi^+}$ (fm)	$r_q^p$ (fm)	$\gamma_\pi$ (fm)	$\gamma_p$ (fm)	$\chi^2/\text{DOF}$
0.025-0.620 <sup>a</sup>	30.63 ± 0.17	29.97 ± 0.16	80.19 ± 0.27	0.37 ± 0.01	0.37 ± 0.01	0.43 ± 0.01	0.65 ± 0.02	0.77 ± 0.05	446.9 370
0.025-0.620 <sup>b</sup>	29.89 ± 0.12	29.48 ± 0.12	80.31 ± 0.25	0.42 ± 0.01	0.42 ± 0.01	0.42 ± 0.01	0.55 ± 0.01	0.77 ± 0.01	510.3 372
0.025-0.320 <sup>a</sup>	30.81 ± 0.25	30.25 ± 0.24	79.28 ± 0.37	0.35 ± 0.03	0.35 ± 0.03	0.46 ± 0.02	0.69 ± 0.03	0.75 ± 0.01	243.8 239
0.025-0.320 <sup>b</sup>	30.34 ± 0.15	29.87 ± 0.15	79.97 ± 0.31	0.41 ± 0.01	0.41 ± 0.01	0.41 ± 0.01	0.58 ± 0.01	0.78 ± 0.01	257.6 240

<sup>a</sup> $\gamma_\pi$ ,  $\gamma_p$  each set to a single value for pion and proton data.

<sup>b</sup> $r_q^{\pi^-}$ ,  $r_q^{\pi^+}$ ,  $r_q^p$  constrained to be equal for pion and proton data.

$r_p$  and  $r_\pi$  are in remarkably good agreement with measured proton<sup>22</sup> and pion<sup>23</sup> electromagnetic charge radii. These fits give  $u/2 = 0.80$  (GeV/c)<sup>2</sup>: thus the quadratic expression goes to zero at  $-t = 1.2$  (GeV/c)<sup>2</sup>. This is close to the dip at  $-t \sim 1.5$  (GeV/c)<sup>2</sup> seen by Akerlof *et al.*<sup>3</sup> in their 200-GeV/c  $pp$  cross section.

The fits using the exponential form for the matrix element (Table X) were made using the full  $t$  range and a restricted  $t$  range [ $0.025 < -t < 0.320$  (GeV/c)<sup>2</sup>]. Over the restricted  $t$  range, reasonable fits to the data were obtained. Over the full range the fits are somewhat poorer, and the value of  $r_p$  is about 10% lower than measurements of the proton electromagnetic charge radius.

Within the context of the above picture, one expects the proton electromagnetic charge radius to be the same whether extracted from the  $\pi^+p$  data or from the  $pp$  data and similarly for the pion electromagnetic charge radius whether extracted from the  $\pi^+p$  or  $\pi^-p$  data. Therefore, we fit the  $\pi^-p$ ,  $\pi^+p$ , and  $pp$  data simultaneously using a single  $r_\pi$  and  $r_p$ ; in some fits the  $r_q$ 's were required to be equal, in some the  $r_q$ 's were allowed to vary independently. Fitting to the  $\pi^-p$ ,  $\pi^+p$ , and  $pp$  data simultaneously also reduced the correlation between the fitted parameters. As the ex-

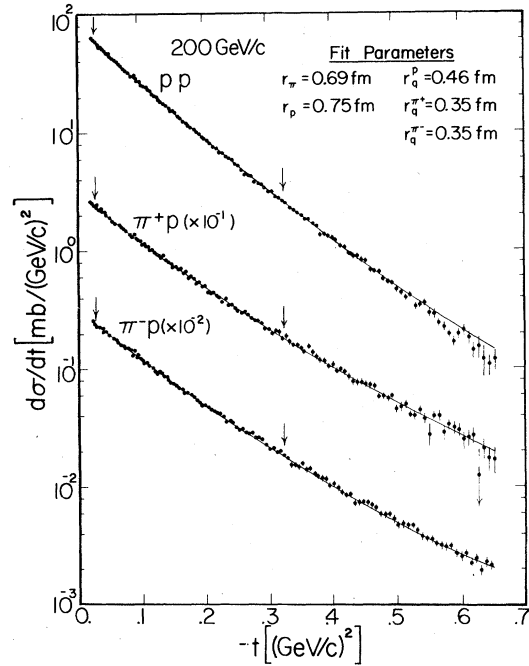


FIG. 14. Results from fits to  $\pi^-p$ ,  $\pi^+p$ , and  $pp$  simultaneously using Eqs. (10) and (11b). Arrows indicate the region of  $-t$  used in the fits. The  $\pi^+p$  and  $\pi^-p$  data have been multiplied by the indicated powers of 10 for clarity.

ponential form of the matrix element [Eq. (11b)] has physical motivation, only the results of the fits using this form are presented in Table XI. Figure 14 shows the results using an exponential matrix element and fitting the data over the region  $0.025 \leq -t \leq 0.320$  (GeV/c)<sup>2</sup>.

We note from Table XI that the fit to the data over the full  $t$  range allowing the  $r_q$ 's to vary independently is reasonable and would indicate  $r_q^p > r_q^\pi$ . The fit constraining the quark radii to be the same in the proton and pion exhibit a somewhat poorer fit. In both cases the values of  $r_p$  are about 5% low when compared to measurements of the proton electromagnetic charge radius.

Over the region  $0.025 < -t < 0.320$  (GeV/c)<sup>2</sup> the data are well represented by the fits using the exponential matrix element. This conclusion is true whether the  $r_q$ 's are constrained to be equal or are allowed to vary independently (though with indepen-

dent  $r_q$ 's the fit is slightly improved). Again  $r_p$  is approximately 5% low when compared to measurements of the proton electromagnetic charge radius.

We are impressed with the general qualitative agreement of our  $\pi^+p$  and  $pp$  elastic-scattering data and the AQM. Our fit results show that the shape of  $d\sigma/dt$  in the region  $0.025 < -t < 0.620$  (GeV/c)<sup>2</sup> is described by a product of the electromagnetic form factors of the projectile and the target and a simple matrix element. This is especially true in the region  $0.025 < -t < 0.320$  (GeV/c)<sup>2</sup>. The fitted values for  $r_p$  and  $r_\pi$  are remarkably close to their electromagnetic counterparts. Within the context of the AQM this is evidence that the hadronic form factors of the pion and proton are very similar to their electromagnetic form factors. The fitted value of the clothed-quark radius is correlated with  $r_p$  and  $r_\pi$  but seems to be between 0.35 and 0.45 fm.

We do not claim that our analysis tests the above theoretical ideas in a strict sense. First Eq. (10) represents only the first-order form for  $d\sigma/dt$ ; higher-order terms have been neglected. Also, there are technical difficulties with the fitting procedure since the results are very sensitive to the values of the proton and pion electromagnetic charge radii. For example, constraining  $r_p$  to be 0.81 fm causes the fit to the  $pp$  data using an exponential matrix element to be quite poor. Thus the uncertainty in the published values of the proton and especially the pion electromagnetic radii are a serious obstacle in further tests of the AQM as applied to high-statistics elastic-scattering data.

#### TESTS OF UNITARITY BOUNDS

Upper limits on the ratio of the scattering amplitude at a given  $t$  to the scattering amplitude at  $t=0$  can be derived. These limits assume unitarity and analyticity of the scattering amplitude in the complex  $s$  plane ( $s$  = center-of-mass energy squared). Figure 15 shows how our data compare to one such upper bound, Eq. (1.3) of Ref. 24. It is seen that there is no violation of the bounds; however, the data are close to saturating them. This behavior has also been observed at energies of 20–30 GeV.<sup>25</sup>

S. M. Roy<sup>26</sup> derives the following bound on  $d\sigma/dt$  for pion-nucleon elastic scattering:

$$b(t) \left( \frac{d\sigma}{dt} \Big|_t \right)^{1/2} \geq \frac{b(0)}{2} \left( \frac{d\sigma}{dt} \Big|_0 \right)^{1/2} \times \left[ 3 \left( \frac{d\sigma/dt|_{t_1}}{d\sigma/dt|_0} \right) \left( \frac{b^2(t_1)}{b^2(0)} \right) - 1 \right], \quad (13)$$

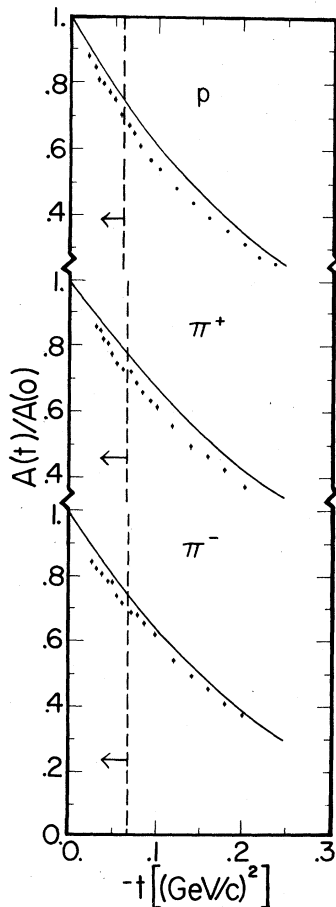


FIG. 15. Comparison of representative results from this experiment (dots) with the upper limit on the ratio of the scattering amplitude at a given  $t$  to the scattering amplitude at  $t=0$ , Eq. (1.3) of Ref. 24 (solid line). The upper limit holds rigorously only to the left of the dashed lines (as shown by the arrow).

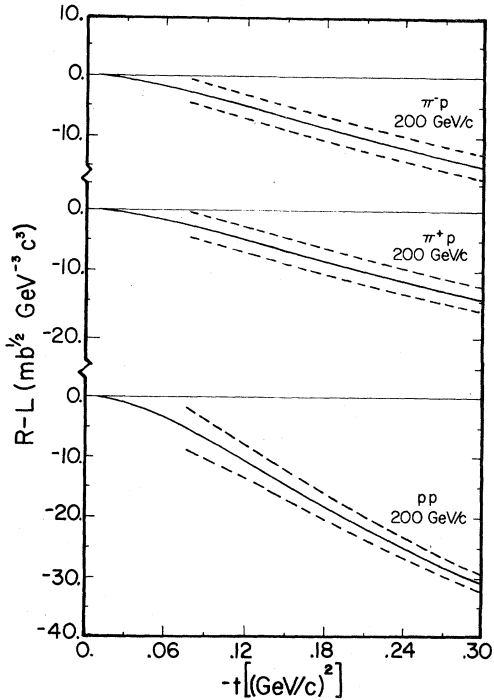


FIG. 16. Right-hand side minus left-hand side of Eq. (13),  $R-L$  (solid line). Dashed lines give  $\pm 1$  standard-deviation error band; error band shown only for  $-t > 0.075$   $(\text{GeV}/c)^2$ .

where

$$t = 3t_1 \left( 1 + \frac{t_1}{4k^2} \right),$$

$k$  = center-of-mass momentum,

$$b(t) = \frac{d\sigma}{dt} [\ln(d\sigma/dt)].$$

In Fig. 16 we plot the right-hand side minus the left-hand side of Eq. (13). [For this study we parametrized the data by Eq. (10) with the quadratic form for the matrix element.] Figure 16 demonstrates that our data satisfy the bound, in contrast to the conclusions of Ref. 26.<sup>17</sup> It is interesting that the bound is not violated for the  $pp$  scattering data; Ref. 26 does not address nucleon-nucleon elastic scattering. Strictly speaking the data test the bound only for  $-t > 0.075$   $(\text{GeV}/c)^2$ . For  $-t \geq 0.25$   $(\text{GeV}/c)^2$  the right-hand side of Eq.

(11) is negative, and the bound is not useful. At  $t = t_1 = 0$  the two sides of the bound are by definition equal; thus at small  $t$  it is not surprising that the bound appears saturated. Finally, it can be shown on general grounds that if  $d\sigma/dt$  is parametrized by Eq. (10) with an exponential matrix element [Eq. (11b)] and  $u$ ,  $r_p$ , and  $r_\pi$  are all greater than zero, then it is impossible to violate the bound at any  $t$ .<sup>13</sup>

#### CONCLUSION

We have measured  $d\sigma/dt$  distributions for  $\pi^-p$ ,  $\pi^+p$ , and  $pp$  elastic scattering in the range  $0.021 < -t < 0.665$   $(\text{GeV}/c)^2$  and studied the shape of these distributions in detail. The variation of the local slope as a function of  $t$  is similar for  $\pi^+p$  and  $\pi^-p$  elastic scattering, while there are indications that the variation is different in  $pp$  elastic scattering.

Over the entire  $t$  range measured,  $d\sigma/dt$  distributions for all three particles are inconsistent with the form of  $e^{bt}$ . However, functional forms involving the product of the electromagnetic form factors of the projectile and the target and a simple matrix element adequately describe the data, especially for  $-t < 0.30$   $(\text{GeV}/c)^2$ . The additive quark model leads to such functional forms for the elastic cross sections. Within the content of this model we estimate the size of the clothed quark in the pion and proton.

Finally, no violations of bounds on the elastic-scattering amplitude were found.

#### ACKNOWLEDGMENTS

We would like to thank the following people for their valuable contributions: Peter Martin, Satish Dhawan, Adrian Disco, Irving Winters, Jon Blomquist, Garvie Hale, and Ed Steigmeyer. We also thank William Frieze for his work on early parts of this experiment. This work was supported in part by the U. S. Department of Energy. One of us (L.R.) was a fellow of the Swiss National Fund for Scientific Research and a second member (L.A.F.) was supported in part by a Ford Foundation Doctoral Fellowship for Mexican-Americans and Puerto Ricans. We also thank A. Bialas and H. Miettinen for a number of stimulating discussions.

\*Present address: Bell Laboratories, Holmdel, New Jersey 07733.

†Present address: Lawrence Berkeley Laboratory, Berkeley, California 94720.

‡Present address: CERN, Geneva, Switzerland.

§Visitor from: Rutherford Laboratory, Chilton, Didcot, Berkshire, England.

||Present address: SLAC, P. O. Box 4349, Stanford, California 94035.

¶Present address: Brookhaven National Laboratory,

- Upton, New York 11973.
- \*\*Present address: Arthur Young and Company, One IBM Plaza, Chicago, Illinois 60611.
- <sup>1</sup>G. Giacomelli, Phys. Rep. 23C, 123 (1976); Istituto di Fisica dell'Universita di Bologna Report No. IFUB 77-12, 1977 (unpublished).
- <sup>2</sup>(a) D. S. Ayres *et al.*, Phys. Rev. D 15, 3105 (1977);  
(b) Fermilab Single Arm Spectrometer Group, Phys. Rev. Lett. 37, 548 (1976).
- <sup>3</sup>C. W. Akerlof *et al.*, Phys. Rev. D 14, 2864 (1976).
- <sup>4</sup>R. K. Carnegie *et al.*, Phys. Lett. 59B, 313 (1975).
- <sup>5</sup>G. Barbiellini *et al.*, Phys. Lett. 39B, 663 (1972).
- <sup>6</sup>J. P. Burg *et al.*, CERN EP Internal Report No. 78-7, 12/14178 (unpublished).
- <sup>7</sup>J. R. Orr and A. L. Read, Meson Laboratory, Preliminary Design Report, 1971, Fermilab (unpublished).
- <sup>8</sup>L. A. Fajardo *et al.*, following paper, Phys. Rev. D 24, 46 (1981); J. Slaughter *et al.* (unpublished).
- <sup>9</sup>S. Dhawan and R. Majka, IEEE Trans. Nucl. Sci. NS-22, 303 (1975).
- <sup>10</sup>M. Sogard, Phys. Rev. D 9, 1486 (1974).
- <sup>11</sup>F. Jenkins *et al.*, Report No. Fermilab-PUB-78/35-EXP (unpublished).
- <sup>12</sup>F. James and M. Roos, CERN Computer 7600 Interim Program Library, D506 and D516 (unpublished).
- <sup>13</sup>A. Schiz, thesis, Yale University (unpublished).
- <sup>14</sup>V. Bartenev *et al.*, Phys. Rev. Lett. 31, 1088 (1973).
- <sup>15</sup>R. Schamberger, Jr. *et al.*, Phys. Rev. D 17, 1268 (1978).
- <sup>16</sup>G. Hohler *et al.*, Institut fur Theoretische Kernphysik Report No. TKP 79-4, 1979 (unpublished).
- <sup>17</sup>G. Hohler *et al.*, Phys. Lett. 86B, 383 (1979).
- <sup>18</sup>T. T. Chou and C. N. Yang, Phys. Rev. 170, 1591 (1968).
- <sup>19</sup>A. Bialas *et al.*, Acta Phys. Pol. B8, 855 (1977); N. W. Dean, Phys. Rev. D 1, 2703 (1970).
- <sup>20</sup>H. J. Lipkin *et al.*, Phys. Rev. 152, 1375 (1966); J. J. J. Kokkedee and L. Van Hove, Nuovo Cimento 42, 711 (1966); E. M. Levin and V. M. Shekhter, Leningrad Nuclear Physics Institute report, 1980 (unpublished); E. M. Levin and V. M. Shekhter, in *Proceedings of the IXth Winter LNPI School on Nuclear Physics and Elementary Particles, Leningrad, 1974* (Akademiya Nauk SSSR, Leningrad, 1974), Vol. III.
- <sup>21</sup>The quark-quark scattering amplitude is written in impact-parameter space ( $b$  space) as  $\exp(b^2/r_q^2)$  (private communication, H. Miettinen). A similar parametrization is used in Ref. 19.
- <sup>22</sup>D. A. Andrews *et al.*, J. Phys. G 3, L91 (1977) and references therein.
- <sup>23</sup>A. Quenzer *et al.*, Phys. Lett. 76B, 512 (1978) and references therein.
- <sup>24</sup>V. Singh and S. M. Roy, Phys. Rev. Lett. 24, 28 (1970). For more detail, see V. Singh and S. M. Roy, Phys. Rev. D 1, 2638 (1970).
- <sup>25</sup>S. M. Roy, Phys. Rep. 5C, 125 (1972).
- <sup>26</sup>S. M. Roy, Phys. Rev. Lett. 43, 19 (1979).